Postseismic afterslip 30 years after the 1978 Tabas-e-Golshan (Iran) earthquake: observations and implications for the geological evolution of thrust belts

Alex Copley

COMET+, Bullard Labs, Department of Earth Sciences, University of Cambridge, Cambridge, UK. E-mail: acc41@cam.ac.uk

SUMMARY

This paper presents InSAR observations of postseismic afterslip occurring up to 30 yr after the M_w 7.3 1978 Tabas-e-Golshan thrust-faulting earthquake in eastern Iran. Comparison of the surface motion from 1996 to 1999 with that from 2003 to 2010, along with information provided by the Quaternary-averaged slip rates of faults in the region, suggests that the imaged slip is transient and decaying through time. Models of the surface deformation field imply slip on faults dipping at $55 \pm 10°$, reaching from the surface to depths of 4–5 km, and slipping at 5 ± 1 mm yr^{-1}. These faults outcrop on the margins of low anticlinal hills composed of actively uplifting Neogene deposits. When compared with the previously studied main shock focal parameters (slip on a plane dipping at $16 \pm 5°$ with a centroid depth of $\sim$9 km), and the aftershock distribution (a band at $\sim$6–14 km), the InSAR results imply postseismic slip on a high-angle thrust ramp connecting the surface anticlines to the coseismic low-angle fault plane at depth. In one location, both a thrust ramp and also a backthrust are postseismically active. The InSAR observations demonstrate the role of postseismic afterslip in the growth of these commonly observed thrust belt geometries, and highlight that deformation throughout the seismic cycle can contribute to the geological evolution of regions of active faulting.

Key words: Satellite geodesy; Rheology and friction of fault zones; Continental neotectonics; Tectonics and landscape evolution.

1 INTRODUCTION

A variety of field, seismological and geodetic observations have been used to suggest that many earthquakes result in fault slip that decreases in magnitude towards the Earth's surface, or remains buried at depth (e.g. Yielding *et al.* 1981; Stein & King 1984; Philip *et al.* 1992; Wald *et al.* 1996; Meyer *et al.* 1998; Jonsson *et al.* 2002; Talebian *et al.* 2004; Fialko 2004; Johanson *et al.* 2006; Johanson & Burgmann 2010; Copley *et al.* 2012). Over repeated seismic cycles, these gradients of slip within the seismogenic layer must be relaxed, either by continued slip on the fault plane, future earthquakes with different distributions of slip, or by off-fault deformation, otherwise large and physically unrealistic elastic strains would accumulate within the rocks bounding the fault zone. This paper presents InSAR observations of shallow postseismic afterslip between 1996 and 2010, following the 1978 M_w 7.3 Tabas-e-Golshan thrust-faulting earthquake in eastern Iran (hereafter referred to as the Tabas earthquake). The earthquake slip was mostly concentrated at depth (e.g. deeper than $\sim$6 km; Berberian 1982; Walker *et al.* 2003), so the shallow afterslip is at least partly accommodating the coseismic displacement gradient. One reason for studying this postseismic deformation is that the extreme length of the afterslip compared with the timescales of months to years often observed (e.g. Savage *et al.* 2005) represents a significant addition to our knowledge of the range of postseismic phenomena that occur.

A further reason for studying the postseismic motions following the Tabas earthquake relates to gaining a greater understanding of the formation and evolution of geological and geomorphological structures in regions of active thrusting. In numerous locations worldwide, the geomorphology and geology associated with active thrust faulting has been examined in detail (e.g. Avouac *et al.* 1993; Burbank *et al.* 1996; Meyer *et al.* 1998; Bayasgalan *et al.* 1999b; Allmendinger & Shaw 2000; Lavé & Avouac 2000; Keller & Pinter 2002; Scharer *et al.* 2006; Charreau *et al.* 2008). Common features include both thrust faults reaching the surface, and also young folds rising from alluvial fans on range margins. By comparing the postseismic motions at Tabas with previous work on the coseismic deformation (Berberian 1979), the distribution of aftershocks (Berberian 1982), and the history of longer term tectonics preserved in the landscape (Walker *et al.* 2003, 2013), it is possible to draw conclusions about the tectonic role of the postseismic afterslip, and the creation of geological and geomorphological features by this and similar seismic cycles.

This paper initially summarises what is currently known about the Tabas thrust system, then describes and interprets InSAR observations of postseismic surface motions resulting from slip on faults in the epicentral region of the 1978 earthquake. The nature of the signal and its evolution through time will be described, followed by an analysis of the causative fault slip. The role of this afterslip in the tectonic evolution of the fault system, and the unusually long timescale of the deformation, will then be discussed.

2 ACTIVE TECTONICS OF THE TABAS REGION

The 1978 Tabas earthquake occurred on a thrust fault in eastern Iran (Fig. 1a), in a location that has experienced multiple phases of extension and compression dating back to the Palaeozoic (Berberian 1979). The present phase of deformation is characterized in the geology and geomorphology by faulted and folded Neogene basin deposits being uplifted along low (less than 100 m high) anticlinal ridges rising out of the surrounding alluvial fans (Walker *et al.* 2003, marked with white arrows in Figs 1b and 2a). A geological cross-section through one of these structures, marked by the yellow oval in Fig. 1(b), revealed a ∼4 km wide fold with distributed internal faulting (Walker *et al.* 2013). The dramatic range front of the Shotori mountains (Fig. 1b) shows evidence of recent strike-slip faulting (Walker *et al.* 2013), but the location of active shortening at the surface is thought to have migrated during the Neogene to the growing folds to the west.

The analysis of *P* and *SH* seismic waveforms shows that the 1978 main shock ruptured a low-angle plane (i.e. $16 \pm 5°$) with a slip vector roughly perpendicular to the strike of the Shotori mountain range (Walker *et al.* 2003). The focal mechanism shown in Fig. 1

is plotted at the hypocentre location estimated by Engdahl *et al.* (1998), and when compared with the distribution of aftershocks, (Berberian 1982, Fig. 1b) implies the event ruptured to the northwest. The coseismic surface deformation described by Berberian (1979) took the form of widely distributed cracking and bedding plane slip, steeply dipping ruptures within the anticlinal hills (at least some of which are thought to be surficial normal faults within the hangingwall of the coseismic thrust fault; Walker *et al.* 2003), and some thrust ruptures with up to ∼35 cm of motion along the western margins of the folds (with the upthrown side on the NE). The low amount of slip compared with the metres expected for an $M_w 7.3$ event implies that most of the slip remained buried at depth, and failed to reach the surface. The surface deformation features were discontinuous along the ∼85 km length of the rupture zone, and the main locations of deformation observed in 1978 are marked as black lines in Fig. 1(b). The centroid depth of the earthquake was estimated at ∼9 km (Walker *et al.* 2003), at a similar depth to the main concentration of aftershocks measured from 12–42 days after the earthquake using locally deployed seismometers (6–14 km; Berberian 1982). The main concentration of aftershocks (marked as black circles in Fig. 1b) was in the region between the Shotori mountains and the western limit of recent surface folding, suggesting that the main shock slip occurred in this region.

Taken together, the existing observations of the 1978 Tabas earthquake have been used to suggest that rupture on a low-angle plane at depth between the Shotori mountains and the anticlinal ridges largely failed to reach the surface, which was coseismically folded and fractured due to the slip gradient along the fault (Berberian 1979, 1982; Walker *et al.* 2003, 2013). The agreement in location between the coseismic surface deformation, and the Neogene to present-day folding and faulting in the low anticlinal hills, suggests that seismic cycles of the same style as that which included the 1978
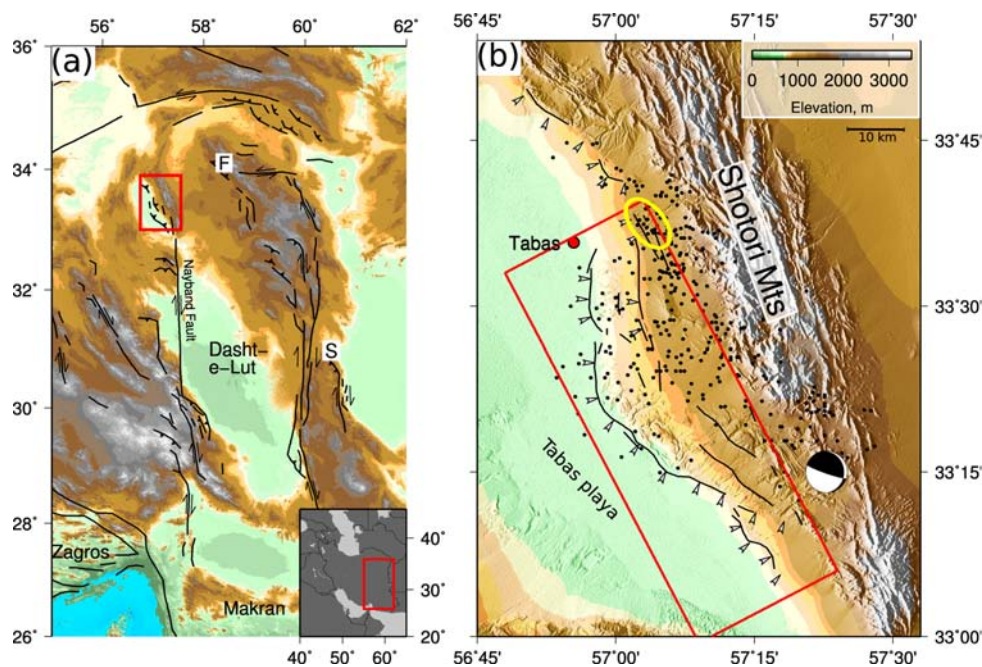
Figure 1. (a) Active faults in eastern Iran (from Walker *et al.* 2003). The area of coverage is shown by the box on the inset. The red box at the northern end of the Nayband fault shows the Tabs region. 'F' and 'S' show the Ferdows and Sefidabeh faults, discussed in the text. (b) Topography of the area inside the red box on (a). Black lines show areas of surface deformation during the 1978 Tabas earthquake (Berberian 1979), and black dots show the locations of aftershocks (Berberian 1982). Small white arrows mark the western edges of a series of low anticlinal hills which are actively uplifting Neogene deposits (Walker *et al.* 2003). The focal mechanism estimated by Walker *et al.* (2003) using body-waveform modelling is plotted at the location of the hypocentre in the catalogue of Engdahl *et al.* (1998). The red box shows the area of coverage of Fig. 2. The yellow oval shows the fold segment studied by Walker *et al.* (2013).
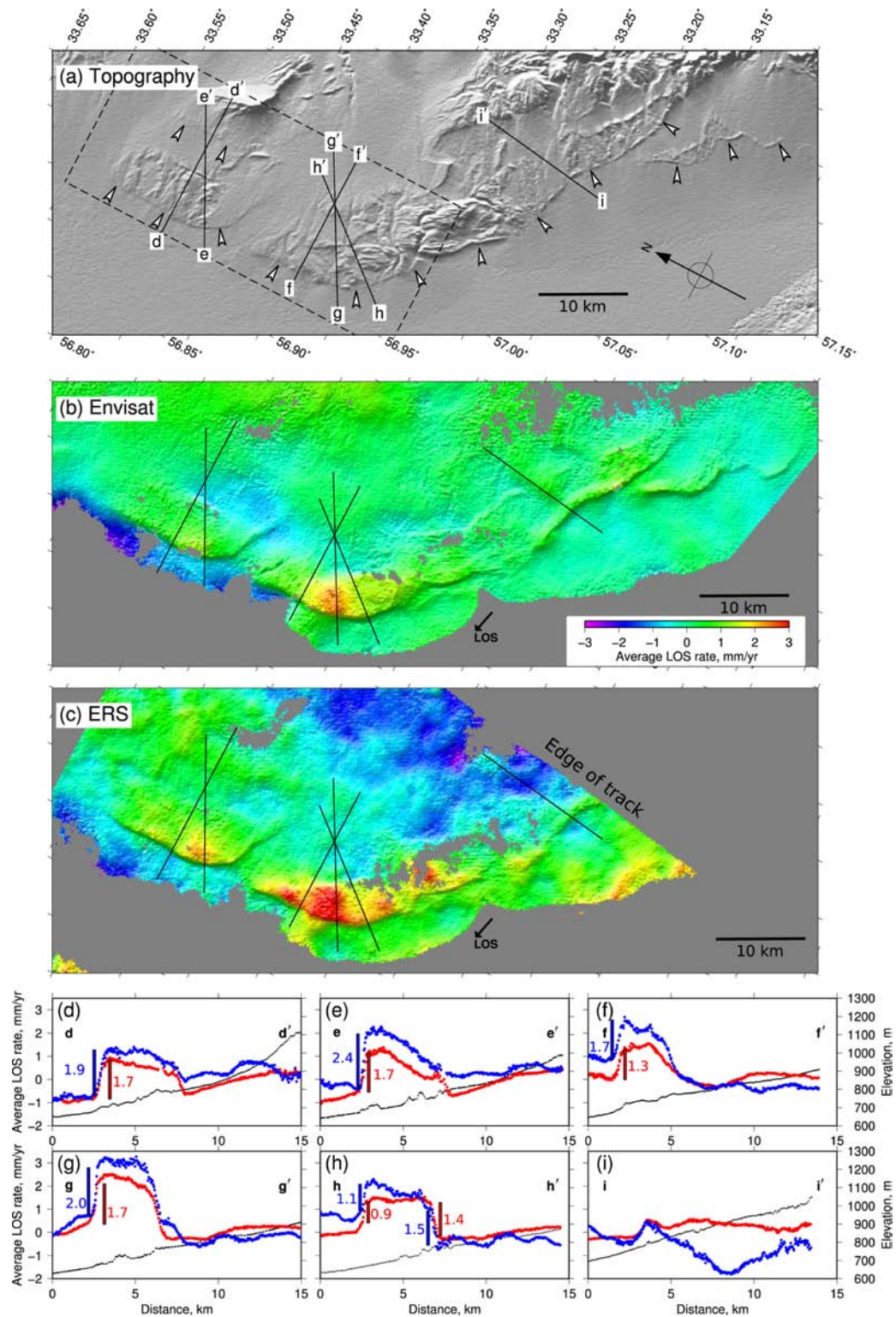
Figure 2. (a) SRTM topography in the region marked by the red box in Fig. 1(b), illuminated from the northeast. Small white arrows mark the western edges of a series of low anticlinal hills which are actively uplifting Neogene deposits (Walker *et al.* 2003). The black dashed box shows the area of coverage of Fig. 3. The absolute elevation of the topography can be seen in Fig. 1(b) and the topographic profiles on panels d–i. (b and c) stacks of interferograms made using Envisat and ERS data, expressed as the average rate of line-of-sight range change during the observation period. Positive rates correspond to motion towards the satellite. The satellite line-of-sight is inclined at $23°$ from the vertical in the azimuth shown by the arrow marked 'LOS'. The interferograms have been plotted as a 3-D surface (viewed from above) and illuminated from the northeast to help identify the displacement discontinuities (the elongated shaded areas). The shading essentially represents the displacement gradient in a NE–SW direction, with dark shading corresponding to displacement increasing to the NE. Areas with strong shading but little colour change represent sharp, but small, displacement jumps. (d–i) profiles of topography (black), motions from the stack of Envisat data (red) and ERS data (blue) along the lines labelled in (a) and also shown in (b) and (c). Where sharp offsets are identifiable, the velocity change across the offset is indicated with a coloured bar (plotted to the side of the actual location of the signal), and the magnitude of the offset is given.

Table 1. Details of the interferograms used in this study.

Scene 1 date (yyyymmdd)	Scene 2 date (yyyymmdd)	Satellite	Track #	Perpendicular baseline (m)	Duration (years)
Descending tracks					
19960513	19980901	ERS1&2	206	−219	2.3
19960513	19990608	ERS1&2	206	−109	3.1
19960514	19980901	ERS2	206	−54	2.3
19960514	19990608	ERS2	206	58	3.1
19960530	19980813	ERS2	435	506	2.2
19960530	19990311	ERS2	435	332	2.8
19960530	19990520	ERS2	435	301	3.0
20030320	20050915	Envisat	435	−58	2.5
20030320	20091203	Envisat	435	−156	6.7
20030911	20051020	Envisat	435	−98	2.1
20030911	20090924	Envisat	435	215	6.0
20040304	20060309	Envisat	435	134	2.0
20040304	20091029	Envisat	435	180	5.7
20041209	20100107	Envisat	435	22	5.1
20050915	20091203	Envisat	435	−108	4.2
20050915	20100107	Envisat	435	−176	4.3
20051020	20090924	Envisat	435	314	3.9
20060309	20091029	Envisat	435	46	3.6
Ascending track					
20040109	20061020	Envisat	156	−30	2.8
20040109	20071005	Envisat	156	−69	3.7
20061020	20071005	Envisat	156	−39	0.9

event govern the geological and geomorphological development of the region. However, an outstanding question which is addressed in this paper concerns how the decrease in slip towards the surface during the 1978 event is accommodated at other times within the seismic cycle. Addressing this question means investigating how seismic cycles result in the development of topographic and geological structures (e.g. King *et al.* 1988), and the similarity between the Tabas fault zone and others studied in a variety of regions (e.g. the Tien Shan, Tibet, Mongolia and California; Avouac *et al.* 1993; Meyer *et al.* 1998; Bayasgalan *et al.* 1999b; Keller *et al.* 1999) means the results presented here have potential implications for a range of thrust belts worldwide.

3 INSAR OBSERVATIONS

3.1 Spatial pattern of the motions

This paper uses data from the ERS 1 & 2 and Envisat satellites, acquired between 1996 and 2010. The SAR data are from ERS descending track numbers 206 and 435 (which overlap in the Tabas region) and Envisat descending track number 435. The interferograms were multilooked to four looks, and made and unwrapped using the Caltech/JPL ROI-PAC software (Rosen *et al.* 2004). The details of the interferograms used are given in Table 1. In order to improve the signal-to-noise ratio in the InSAR results, multiple unwrapped interferograms were stacked. Such a procedure reinforces spatially consistent motions (such as those expected for tectonic deformation), and reduces the influence of noise that varies spatially between individual interferograms (e.g. Wright *et al.* 2001; Fialko 2006). Fig. 2(c) shows a stack of seven ERS interferograms from within the time interval 1996 May 13 to 1999 May 20 which, when the lengths of the individual interferograms are added together, has a cumulative observation time of 21.7 yr. Fig. 2(b) shows a stack of 11 Envisat interferograms from between 2003 March 20 and

2010 January 7, with a cumulative observation time of 46.2 yr. The cumulative perpendicular baseline for the Envisat stack is 315 m, and for the ERS stack is 815 m. Although the cumulative ERS perpendicular baseline is quite large, the results do not significantly change if a large-baseline interferogram is removed, and the cumulative baseline reduces to 309 m. Due to the stable and unvegetated ground surface, even the longest individual interferograms possible given the data acquisition dates (∼6 yr) show excellent coherence in all areas except the playa in the valley to the west of the Tabas faults and folds (the grey area in Figs 2b and c). Some discontinuous coherent areas were visible in the playa region, showing signals with 5–10 km wavelengths, which due to their location are likely to be hydrological in origin. However, the discontinuous nature of the coherent patches meant that they could not be unwrapped with the rest of the data, so they are not shown in Fig. 2.

Because they are formed from stacks of interferograms, the results shown in Fig. 2 represent the average rate of motion in the satellite line-of-sight (inclined at 23° from the vertical, and in the direction marked on the figure) over the time interval covered by the stacks, weighted by the number of interferograms covering a given time. The interferograms we use are fairly evenly distributed in time, so the displayed stacks of interferograms approximate the average rate over the total time interval of the stacks. Both tectonic and non-tectonic signals are present in the InSAR results. The gentle gradients with wavelengths of >1 km and amplitudes of up to 2 mm yr^{-1}, but mostly 1 mm yr^{-1} or less, are likely to be related to atmospheric effects. However, the most striking features of the InSAR results are the sharp discontinuities coinciding with the locations of the low anticline ridges where surface deformation occurred during the 1978 earthquake. These signals correspond to motion towards the satellite in the interiors of the anticlines, and are of higher amplitudes and shorter wavelengths than any other signals present in the InSAR results shown in Fig. 2. The following lines of reasoning suggest that these discontinuities, clearly visible on the profiles through the stacked interferograms shown in Figs 2(d)–(i), represent
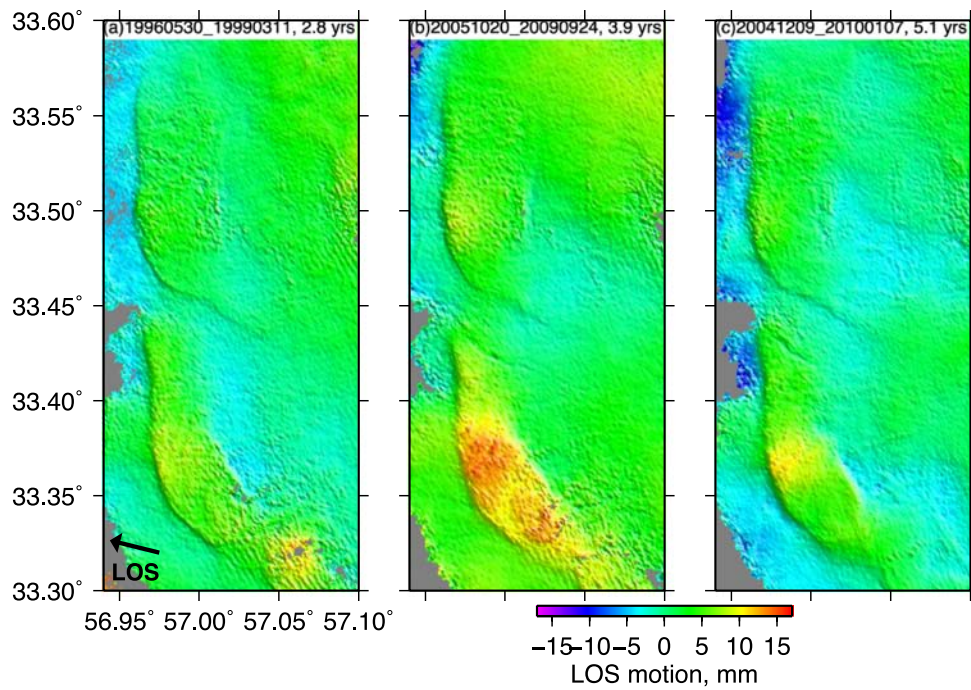
Figure 3. Examples of the individual interferograms used in this study, covering the area within the black dashed box in Fig. 2(a). The three examples were chosen to include a range of interferogram timespans, and were constructed using independent data from both the ERS2 (panel a) and Envisat (b and c) satellites. The interferograms are labelled with the dates of the two data acquisitions used (in the format YYYYMMDD), and the satellite line-of-sight is marked on panel (a). Positive motions correspond to motion towards the satellite. The interferograms have been plotted as a 3-D surface (viewed from above) and illuminated from the northeast, as described for Fig. 2. The comparison of (b) and (c) demonstrates the presence of long-wavelength features in the InSAR results that vary between interferograms (which appear as a DC-shift on a view this size, making the displacements in (c) appear more negative than in (b)). However, the tectonic motions we interpret are present in the individual interferograms, superimposed upon this changeable background.

tectonic motion. First, the signals are present on all of the individual interferograms that formed the stacked results, which involve numerous different combinations of independent scenes (Table 1). This consistency is in contrast to the longer wavelength signals, whose shifting locations and signs in the individual interferograms suggest an atmospheric origin. Examples of three of the individual interferograms are shown in Fig. 3. These three interferograms are representative of the others used in this study, were chosen to include a range of interferogram time-spans and are constructed using independent data from both the ERS2 (panel a) and Envisat (b and c) satellites. The second reason why the sharp discontinuities in the InSAR results are likely to be tectonic in origin is that the anticlinal ridges where they are situated are less than 100 m high, so are unlikely to be a source of topographically correlated atmospheric signals. This point is corroborated by the fact that the ∼2900 m high Shotori mountains to the east produced atmospherically correlated signals that are only present in some of the individual interferograms, and are smaller than the tectonic motions discussed here. Third, incision of drainage has dissected the anticlinal ridges, and although the InSAR signal lies over the general area of these ridges, it does not correlate with the actual topography within them (see black topographic profiles along with the InSAR signal in Figs 2d–i). Fourth, the presence of the signals on interferograms constructed with a range of perpendicular baseline lengths and signs (including one of 22 m, as shown in Fig. 3c, the shortest available given the acquired data), implies that elevation model errors are not likely to be the source of the signal. Finally, the constant sign of the signal throughout our observation period, the lack of visible seasonal dependence, the distinctive shape of the deformation pattern (described in more detail below) and the presence of the signal only

in the area of the Tabas earthquake, and not the geologically and climatologically similar regions along-strike of the range, suggest that hydrological effects are not the cause of the surface motions. Taken together, these characteristics of the signal suggest that the sharp discontinuities corresponding to the location of the anticlinal ridges in Fig. 2 represent tectonic motion.

Three mechanisms have been commonly observed to cause postseismic ground motions. Poroelastic relaxation generally occurs on timescales of months, and produces relatively smooth displacement signals at the surface. The decadal timescale of the signal shown in Fig. 2 and the sharp discontinuities in the signal rule out this mechanism as the source of the deformation. Viscoelastic flow at depth and afterslip on the deep parts of fault zones also result in smoothly varying displacement signals at the surface, because the motions are transmitted through the elastic upper crust. The postseismic mechanism which is consistent with the signal in Fig. 2 is therefore slip on shallow faults, breaking the surface or reaching close to it. In the following sections, the observed displacements will therefore be analysed from the perspective of postseismic afterslip on faults.

In some places, the displacement discontinuity due to the fault slip is unresolvably sharp on the interferograms (multilooked to four looks), while in others, it is spread over a distance of hundreds of metres. These length scales imply that the faulting reaches the surface, or close to it. However, we are unaware of any studies that have attempted to observe in the field any postseismic faulting in the Tabas region, and such work is beyond the scope of this study.

In addition to the data gathered by the satellites on descending tracks, there are three Envisat data acquisitions available from ascending track number 156, which also covers the Tabas region (Table 1). The small amount of data relative to that included in
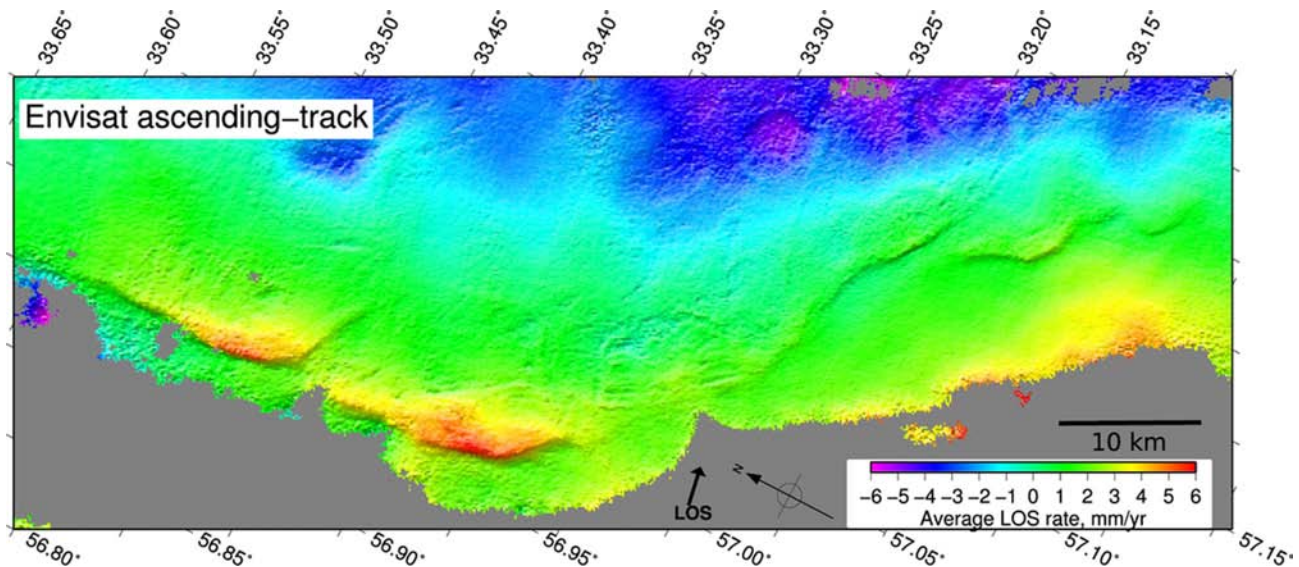
Figure 4. As Figs 2(b) and (c), but for the ascending-track Envisat data. The ascending-track line-of-sight (LOS) is shown.

the stacks described above (resulting in three interferograms with a cumulative observation time of 7.5 yr) makes the results more noisy, and there is a topographically correlated signal present over the Shotori Mountains. However, the tectonic motions described above are present in the data, with a larger magnitude than the topographically correlated signal (Fig. 4). The tectonic motion has the same sense as in the descending-track data (i.e. motion towards the satellite within the anticlinal ridges). The agreement in sense of motion between the ascending and descending tracks suggests a large vertical component to the ground motion, in agreement with the thrusting mechanism of the main shock (and presumably also the resulting afterslip). Due to the higher levels of non-tectonic noise in the interferograms compared to the descending-track results presented above, the ascending-track motions will not be considered further in this paper. Specifically, the topographically correlated signal results in a gradient in the NE part of the interferogram which is similar to the displacement gradient in the fault hangingwall, so the fault parameters cannot be well-constrained using this data because of the resulting trade-offs.

3.2 Transient or steady-state deformation?

When interpreting the tectonic significance of the deformation signal at Tabas, it is important to establish whether it is transient deformation, or whether we are observing the steady-state creep of the fault zone. Two lines of reasoning can be used to address this question.

Estimates of fault slip rates in eastern Iran over timescales of multiple seismic cycles can be used to infer whether the motions at Tabas are transient or steady-state. The Tabas thrust faults lie at the northern end of the Nayband right-lateral strike-slip fault (Fig. 1a). The Tabas thrust faults, and others in the region such as those at Ferdows (F in Fig. 1), are thought to have total displacements that die out towards their northern ends, and accommodate the termination of the east Iran strike-slip faults by rotations about vertical axes (e.g. Berberian *et al.* 2000). Examples of this style of strike-slip fault termination, which is necessary if the faults do not link to other structures, are also seen in other regions of strike-slip faulting

(e.g. Mongolia; Bayasgalan *et al.* 1999a). In this tectonic model, the long-term slip rate on the thrust faults is required to be the same as the strike-slip fault where the two faults join, and to decrease with distance along the thrust fault. Based on the dating of offset lavas, the Nayband strike-slip fault is estimated to have a slip rate of $1.4 \pm 0.5 \, \text{mm yr}^{-1}$ (averaged over $\sim$2 Ma, which is thought to be younger than the age of initiation of the faulting; Walker *et al.* 2009). The displacement rate in the satellite line-of-sight in the InSAR results from Tabas is $\sim$1–3 mm yr^{-1}. This value represents only one component of the total ground motion, which means that the slip rate on the faults must be higher. Detailed modelling of the faults (described below) suggests slip rates of $5 \pm 1 \, \text{mm yr}^{-1}$, in some cases on a single fault and in others distributed across two parallel faults. This slip rate is higher than the quaternary-averaged rate on the Nayband fault, indicating that it represents transient deformation which will be balanced later in the seismic cycle by slower motions. Additionally, Walker *et al.* (2013) studied a segment of the Tabas fold and thrust system to the north of the segments where postseismic slip is visible (marked by a yellow oval in Fig. 1b), and estimated a Holocene-averaged horizontal shortening rate of $\sim$1.5 mm yr^{-1}. Although there is no visible postseismic motion on that fault segment, it is in a region where there is only one known active structure, implying that the slip rate represents an estimate for the total motion across the entire Tabas thrust belt at that location. The low time-averaged rate of motion compared with that of the slipping faults studied here, which are located as little as $\sim$10 km to the southwest, also suggests that the motion measured with InSAR represents transient postseismic deformation.

An alternative method of examining if the motions are transient or steady state involves comparing the data from the ERS 1 & 2 and Envisat satellites. The stack of ERS data covers an earlier time period than the stack of Envisat data (1996–1999 compared to 2003–2010). If the deformation rate is decaying with time, we would therefore expect the rates of motion measured using the ERS data to be larger than those estimated using the Envisat data. Although the non-tectonic noise in the stacked interferograms is different between the two stacks, this noise has a wavelength of kilometres, rather than the sharp discontinuities due to the fault slip that are visible in the maps of average motion rate shown in Fig. 2. It is therefore

possible to compare the fault displacement rates over the two time periods by comparing the magnitudes of the sharp displacement–rate steps, which are unaffected by the longer wavelength noise. The displacement–rate offsets are identified and the comparison made in Figs 2(d)–(i). The identification of the offsets was made by eye. The choice of the limits of the displacement–rate jumps is slightly subjective, particularly where velocity gradients are present close to the sharp discontinuities. However, the similarity in the shapes of the signals in the ERS and Envisat data means that the measurements can be taken between equivalent points on the two data sets, and any mis-interpretations will be common to both measurements. The comparison between the offsets measured on the ERS and Envisat data shows that the rate discontinuities are consistently larger in the ERS stack (blue in Figs 2d–i) than the Envisat stack (red), suggesting that the rate of motion is decreasing through time and therefore that the fault slip is a transient and decaying postseismic phenomenon. This line of reasoning relies on the identification of the magnitudes of the offsets in the stacked interferograms, so involves a degree of subjectivity. However, the agreement with the conclusions based on the fault slip rates over multiple seismic cycles, as described above, implies that the relative magnitudes of the displacement offsets have been correctly identified.

4 MODELS OF FAULT SLIP

This section describes models of the InSAR-derived surface displacements that have been constructed to constrain the geometries and rates of motion of the causative faults. The non-tectonic noise in the data makes producing models of the 2-D surface deformation field highly problematic. The geometry and rate of the faulting have therefore been estimated by producing models of profiles through the InSAR stacks, constructed perpendicular to the strike of the deformation front. Two profiles have been chosen in which the InSAR signals at the ends of the profile are low, suggesting that the noise level in the locations of these profiles is low. To further minimize the effects of noise in the data, during the inversions an offset of the data relative to zero, and a gradient along the profile, are also inverted for. The profiles selected for modelling are profile e–e′ (from ERS data) and h–h′ (from Envisat data) in Fig. 2.

The profiles have been modelled using the routines of Okada (1985) for constant slip on a rectangular plane. The free parameters in the model are the depth to the top and bottom of the fault plane, the dip and slip rate of the fault, and the along-profile position of the surface projection of the fault. In addition, an offset of the entire profile relative to zero and a gradient along the profile are also modelled in order to minimize the effects of non-tectonic noise on the inversions. The along-strike length of the fault, and the along-strike position of the profile, were fixed based on the location of the profiles relative to the pattern of displacement steps in Fig. 2. The rake was assumed to be pure thrusting. The relatively low number of fault parameters means that it was possible to perform a grid search through the free parameters, and explore the range in each parameter that allows the data to be fit within a given tolerance (the grid search limits and increments are given in Table 2). Fig. 5(a) shows the best-fitting solution for profile e–e′, along with the others from the grid search that had misfits within 50 per cent of the best fit. Histograms in Figs 5(b)–(d) show the range of model parameters that result in misfits within 25 per cent (black) and 50 per cent (grey) of the best fit. Considering the solutions with misfits within 25 per cent of the best fit, these inversions suggest that the surface deformation was caused by an east-dipping fault slipping at 5 ± 1 mm yr^{-1}, reaching

Table 2. Details of the grid search parameters used in the models of the InSAR data. See text for details.

Parameter	Min. value	Max. value	Increment
Profile e–e′			
Slip rate (mm yr^{-1})	2	7	0.5
Depth to base (km)	2	7	1
Depth to top (km)	0	1	0.25
Dip (°)	20	90	5
Location[a] (km)	2	3	0.1
Offset[b] (mm yr^{-1})	−0.6	0.6	0.2
Gradient[c] (mm yr^{-1}/km)	−0.2	0.2	0.025
Profile h–h′			
Offset[b] (mm yr^{-1})	−1	1	0.25
Gradient[c] (mm yr^{-1}/km)	−0.3	0.3	0.1
Left-hand fault:			
Slip rate (mm yr^{-1})	1	5	1
Depth to base (km)	2	14	2
Depth to top (km)	0	0.75	0.25
Dip (°)	20	90	20
Location[a] (km)	1.5	3	0.5
Right-hand fault:			
Slip rate (mm yr^{-1})	1	6	1
Depth to base (km)	2	14	2
Depth to top (km)	0	0.75	0.25
Dip (°)	20	90	20
Location[a] (km)	6	8	0.5

[a]The along-profile position of the projection of the fault plane to the surface.
[b]Offset of the data relative to zero.
[c]Velocity gradient along the profile.

from a depth of 0–0.25 km to ∼4–5 km at the base, with a dip of $55 \pm 10°$. The surface projection of the model fault coincides with the western margin of the low anticlinal ridge.

A similar procedure was undertaken for profile h–h′ (from the Envisat data), with the addition of a second fault plane dipping to the west, which was required to fit the data. This requirement results from the shape of the flat-topped 'hump' on the surface motion profile (Fig. 6), the production of which requires two faults dipping towards each other, one outcropping at each of the sharp displacement jumps. The inversion results are shown in Fig. 6. The grid search was only conducted over fault configurations in which the faults did not cut each other at depth, so pairs of faults that appear to cut each other in Fig. 6(h) are from different inversions. The increased numbers of parameters made the grid search more computationally costly than the analysis of profile e–e′, but this was compensated for by increasing the sampling intervals for the fault parameters (Table 2). There are trade-offs introduced by the presence of two faults. In particular, as the dips of faults approach vertical, the absolute magnitudes of displacement on the footwall and hangingwall sides become more similar. There are therefore a range of model solutions in which steeply dipping faults, reaching up to the maximum depth sampled in the grid search of parameters (14 km), produce surface motion profiles in which the motion due to each fault mostly cancels out in the areas either side of the clear displacement 'hump'. This phenomenon is responsible for the relative insensitivity of the data to the dip and maximum depth of the faults (Fig. 6). If only dips less than 60° are considered, similar to the results from profile e–e′ discussed above, then the maximum depth of faulting is found to be in the 2–7 km range, also similar to
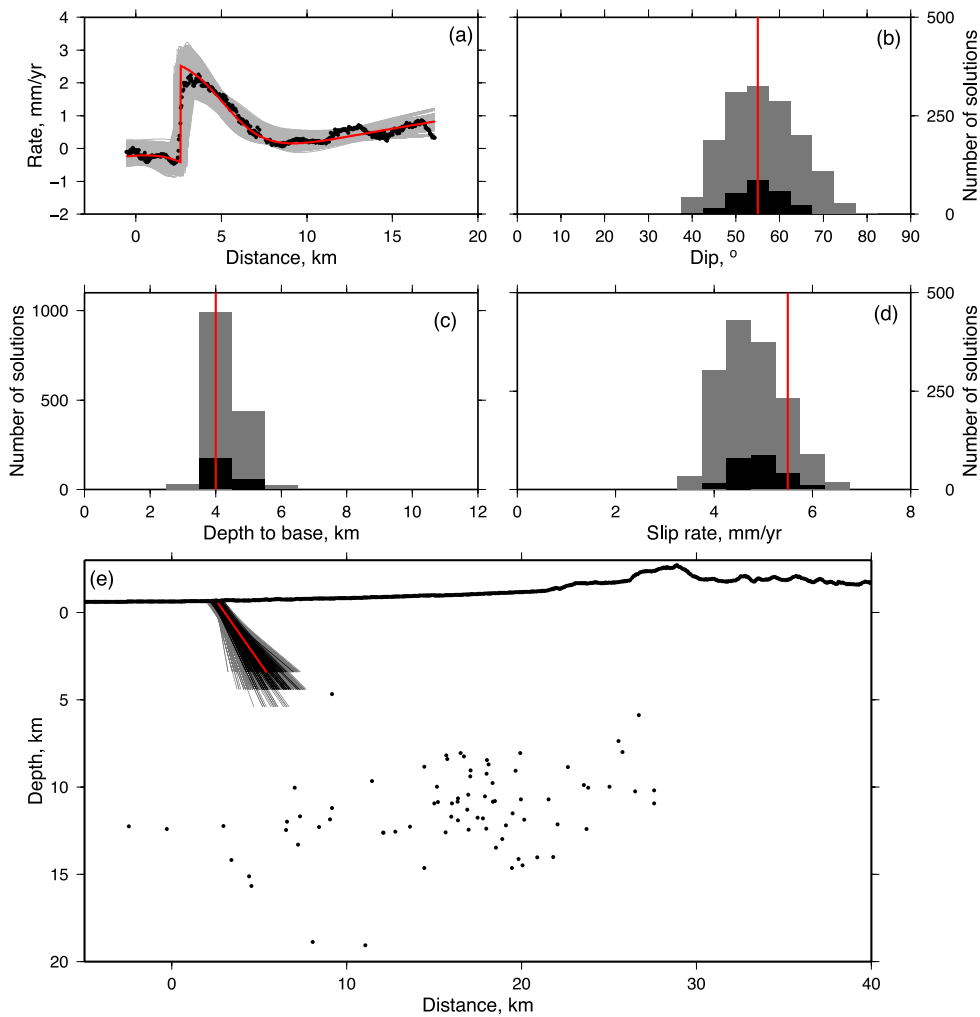
Figure 5. Models of the ground motion along profile e–e′ in Fig. 2, measured using ERS data. (a) Observed motions in the satellite line-of-sight (black points), best-fit model (red line) and models with misfits within 50 per cent of the minimum misfit model (grey lines). (b, c, d) Histograms of dip, depth to base and slip rate of the models that fit the data to within 25 per cent of the minimum misfit model (black) and 50 per cent of the minimum misfit model (grey). The red lines show the parameters of the best-fitting model. (e) Cross-section showing topography (black line), aftershocks of the 1978 Tabas event (black circles, Berberian 1982) and model faults (red: minimum misfit solution, black: misfit within 25 per cent of the minimum misfit model, grey: misfit within 50 per cent of the minimum misfit model).

the estimate from profile e–e′. Although the depth extent of faulting is poorly constrained, the slip rates of both of the faults are found to be in the range ∼2 ± 1 mm yr^{-1}.

Modelling has also been attempted for some profiles that are more affected by non-tectonic motions. Modelling of profile e–e′ using Envisat data produces results that are less well constrained than those from the ERS data, but are consistent with them. Modelling of profile d–d′ using both ERS and Envisat results gives estimates of the fault parameters that are in some cases poorly constrained, but where good estimates can be made they are consistent with the results of the neighbouring profile e–e′. The fault slip rate is one of the most well-constrained parameters in these inversions, due to the dependence of this parameter on the relatively clear sharp displacement jump at the fault, and in all cases it is greater than the quaternary-averaged rate discussed above. The results of these other inversions can be seen in Appendix A.

Since the date of the first InSAR acquisition used in this study, there have been four teleseismically recorded earthquakes within 10 km of the deformation zones observed in the InSAR data, with body-wave magnitudes between 3.8 and 4.4. The total moment

released by the imaged afterslip is approximately 4×10^{17} Nm (equivalent to $M_w \sim 5.7$), assuming a 14 yr observation period, 5 mm yr^{-1} of slip on a 30 km length of faulting reaching from the surface to 4 km depth on faults dipping at 55°, and a shear modulus of 4×10^{10} Pa. The large geodetically derived moment compared with the seismic moment release suggests that the majority of the slip is likely to be aseismic.

5 DISCUSSION

5.1 Tectonic role of the observed afterslip

The model presented above with well-constrained fault parameters for profile e–e′ implies slip on faults that are steeper than the main shock rupture plane (55 ± 10° compared to 16 ± 5°; Walker *et al.* 2003), and also shallower (from the surface to ∼4–5 km, compared to a centroid depth of 9 km, which represents the slip-weighted average depth of the coseismic fault plane). It has been suggested elsewhere (Berberian 1982; Walker *et al.* 2003) that the location of
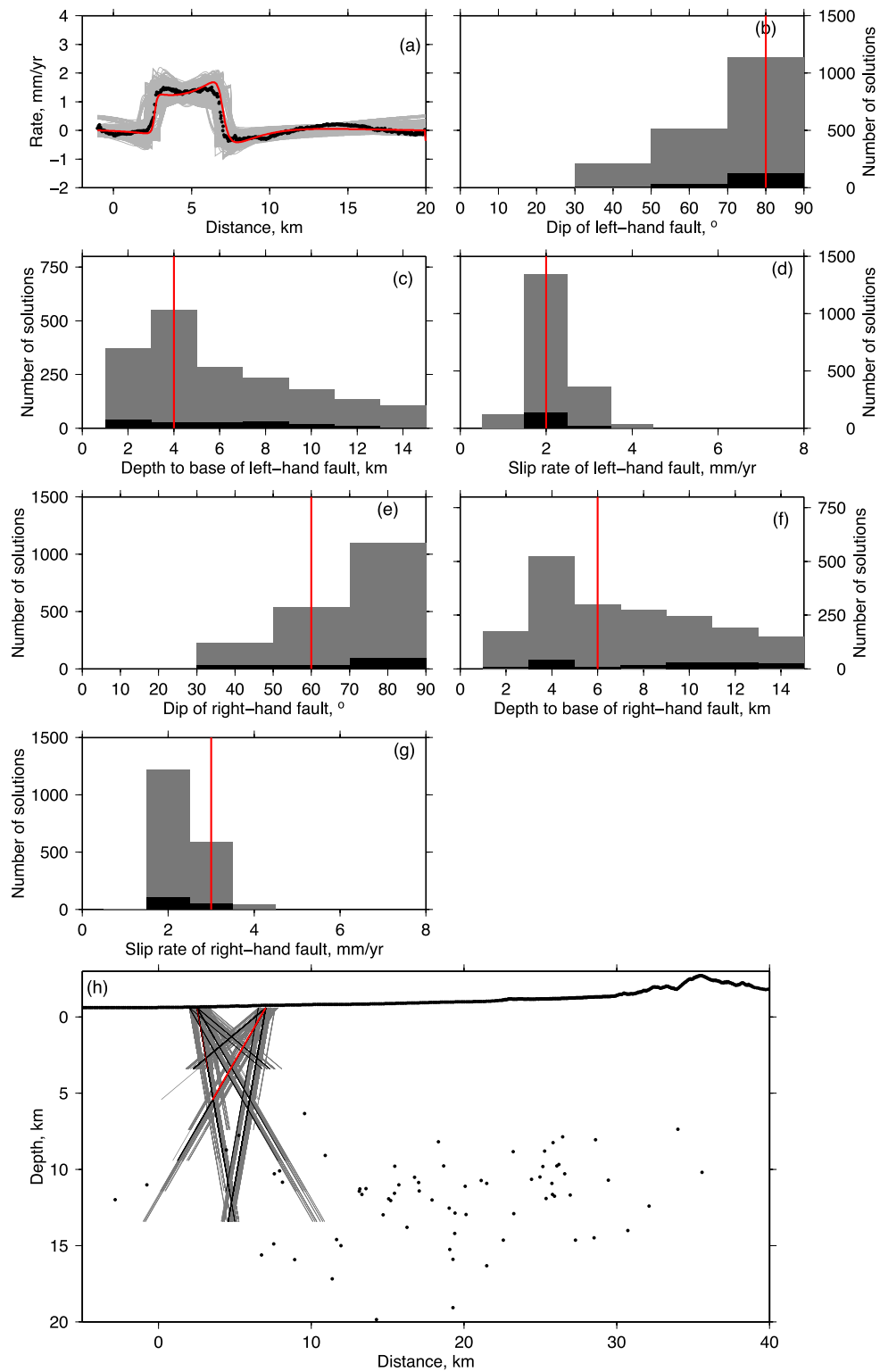
Figure 6. Models of the ground motion in the satellite line-of-sight along profile h–h′ in Fig. 2, measured using Envisat data. (a) Observed motions (black points), best-fit model (red line) and models with misfits within 50 per cent of the minimum misfit model (grey lines). (b–g) Histograms of dip, depth to base and slip rate (for both model faults) of the models that fit the data to within 25 per cent of the minimum misfit model (black) and 50 per cent of the minimum misfit model (grey). The red lines show the parameters of the best-fitting model. (h) Cross-section showing topography (black line), aftershocks of the 1978 Tabas event (black circles, Berberian 1982) and model faults (red: minimum misfit solution, black: misfit within 25 per cent of the minimum misfit model, grey: misfit within 50 per cent of the minimum misfit model).
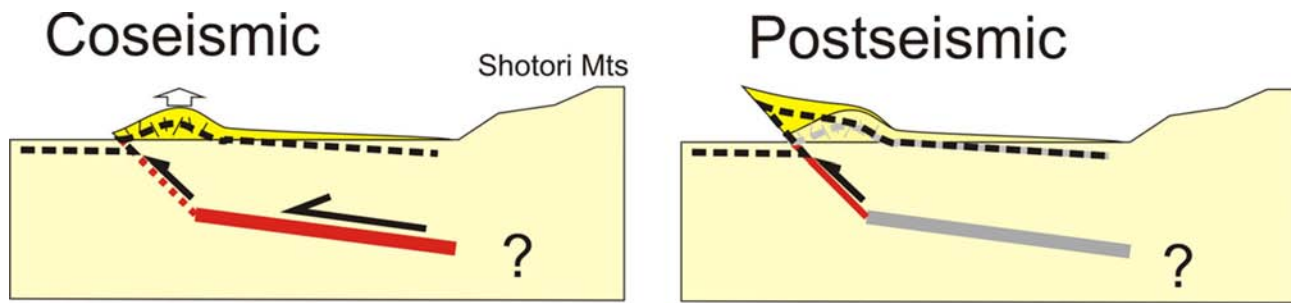
Figure 7. Cartoon to illustrate the sequence of deformation throughout the coseismic and postseismic time periods for the 1978 Tabas earthquake.

the minor coseismic surface deformation within and on the margins of the recent anticlines, and the concentration of aftershocks between these ridges and the Shotori Mountains, suggests that the coseismic rupture dominantly occurred at depth between the Shotori Mountains and the anticlines. Such a location suggests that the postseismic slip studied here occurred near the western edge of the coseismic rupture. The location and dip of the postseismically slipping faults, along with the previous work on the coseismic deformation (Berberian 1979, 1982; Walker *et al.* 2003), allows us to develop a conceptual model for the deformation during the coseismic and postseismic period at Tabas, as illustrated in Fig. 7. Coseismic slip was dominantly concentrated on a low-angle plane (or planes) with a centroid depth of ∼9 km beneath the alluvial apron between the Shotori mountains and the surface anticlines. Coseismic anelastic folding and minor fault slip occurred in the region of the anticlines, but the magnitude of deformation was less than on the low-angle plane at depth (as required by both the low-displacement nature of the coseismic surface deformation and the seismological estimates of the centroid depth and aftershock distribution). At least part of the vertical displacement gradient resulting from the distribution of coseismic deformation is being relieved by slip on higher-angle 'ramps', extending from the surface to depths approaching the top of the coseismic rupture depth. In some places, slip is occurring simultaneously on a NE-dipping fault and a SW-dipping backthrust (as modelled for profile h–h′). This conceptual model is consistent with the style of deformation observed in a transect across an anticline in the Tabas region performed by Walker *et al.* (2013), although no postseismic deformation is visible on the fold segment they studied (marked by a yellow oval in Fig. 1b). Walker *et al.* (2013) observed both folding and faulting in a ∼4-km-wide anticlinal structure. The postseismic observations presented here, along with the prior coseismic work, imply that the folding in such structures may occur coseismically, while the faulting at least partly represents postseismic slip (along with some minor coseismic motion).

The geometry of faulting revealed by comparing the coseismic and postseismic deformation is in agreement with the tectonic interpretation of Berberian (1982) based on the aftershocks of the 1978 event. The concentration of the aftershocks in a subhorizontal band at 6–14 km depths, but the relatively high-angle dips of some of the nodal planes of the shallower-depth events (i.e. >30°), led Berberian (1982) to suggest that these high-angle faults reached from the surface to a low-angle thrust at depth. The postseismic InSAR results have confirmed this structural geometry, and revealed when in the seismic cycle the higher angle thrust ramps are active.

The postseismic observations at Tabas present an insight into the growth and evolution of young fold-thrust belts. As at Tabas, recent deformation often appears to be concentrated on narrow (<5–10 km wide) structures that deform recent sediments and are located out-

board of the main topographic range-front (e.g. Avouac *et al.* 1993; Meyer *et al.* 1998; Bayasgalan *et al.* 1999b; Keller *et al.* 1999). This style and location of shortening has been interpreted to represent the locus of thickening migrating into the footwall of the thrusts that built the main mountain range, probably due to the increases in gravitational energy that accompany the growth of topography making continued slip on the main interface less energetically favourable. In Mongolia, for example, Bayasgalan *et al.* (1999b) suggested that the migration of shortening towards the foreland could be aided by slip on weak horizons (e.g. lake beds) within the sedimentary sequence. The short wavelength of the surface features compared with the seismogenic thickness in such regions, combined in places with information from the surface and subsurface geology, led to suggestions that the faults must flatten at depth, rather than cutting the entire seismogenic layer as a single plane (e.g. Avouac *et al.* 1993; Meyer *et al.* 1998; Bayasgalan *et al.* 1999b; Walker *et al.* 2003; Charreau *et al.* 2008). The combined coseismic and postseismic results from Tabas have observed this style of thrust geometry, and imaged the motion on the 'ramp' faults that connect the surface anticlines to the lower angle fault plane at depth. The postseismic fault slip can therefore be seen to form an important part of the seismic cycle in such regions, and contribute to the structural evolution of thrust belts.

5.2 Timescale of the deformation

One of the remarkable features of the Tabas postseismic deformation is the timescale over which the afterslip has occurred (and is probably still occurring). Studies that have previously described postseismic afterslip commonly observe the motions decaying on timescales of months to years (e.g. Savage *et al.* 2005), rather than continuing for the decades seen here. The long timescale observed at Tabas has two potential causes, as described below.

The first possible cause of the surprisingly long timescale of the deformation relates to the available data and the rates of tectonic motion in the area. The arid regions of eastern Iran commonly have stable land surfaces composed of stoney desert with little vegetation, which results in excellent InSAR coherence (Fig. 2). The Holocene-averaged horizontal shortening rate of the Tabas thrust system is low (e.g. ∼1.5 mm yr^{-1}; Walker *et al.* 2013). When combined, these factors mean that multiple interferograms can be constructed with long temporal baselines, resulting in an excellent signal-to-noise ratio, and there is very little ground motion present from other tectonic motions (e.g. interseismic strain accumulation) or hydrological effects. It may therefore be the case that other fault systems where afterslip has been observed may exhibit postseismic slip on decadal timescales, but that other causes of ground motion (both tectonic and non-tectonic) and less ideal data (either in terms of the noise level

or, in the case of GPS, the spatial sampling) may have resulted in small and long-lasting signals remaining hidden. A possible corroboration of this view is provided by another example of long-term afterslip, following the M_w 9.2 1964 Alaska earthquake. Suito & Freymueller ([2009](#)) observed afterslip continuing for at least 40 yr following the earthquake, at which time the rate was $\sim$1 cm yr^{-1}. In this case, afterslip of up to $\sim$4 m is occurring to relieve the stresses downdip from $\sim$15–20 m of coseismic slip. A total of 95 per cent of the afterslip is estimated to have occurred within 30 yr of the event. Without knowledge of the values of all the parameters that form equations commonly used to model afterslip (e.g. Perfettini & Avouac [2004](#)), it is difficult to establish the functional form of the dependence of the evolution of the fault slip on the initial stress perturbation (which depends on the importance of this term relative to others in the equations). However, we can estimate the rough order of magnitude of the rate of slip expected at Tabas by analogy with the Alaska event if we assume that the scaling with the initial stress change is roughly linear. This estimate is on the order of millimetres to tens of millimetres per year, and is similar to what we have observed, indicating that the Tabas fault may have similar mechanical properties to that which ruptured in the 1964 Alaska earthquake. A further long-lasting afterslip signal has been observed near to Tabas, following the Sefidabeh thrust-faulting earthquake sequence (S in Fig. [1](#)). This earthquake sequence in 1994, with a cumulative moment magnitude of 6.5, resulted in postseismic motions for at least 15 yr (Copley & Reynolds in review), which are likely to be still continuing, also indicating that timescales approaching that seen at Tabas are not unique. Unfortunately, the absence of data from early in the postseismic period at both Sefidabeh and Tabas prevents a more quantitative comparison being made.

An alternative possible explanation for the long timescale observed at Tabas is that the frictional parameters of this fault are unusual. The 2006 M_w 7.0 Mozambique earthquake produced a shallow slip deficit of $\sim$1–3 m (Copley et al. [2012](#)), similar to the likely value at Tabas. In the case of Mozambique, the afterslip driven by this slip gradient had decayed to rates similar to that seen at Tabas within 4 yr of the earthquake, implying different frictional properties for the two faults. Similarly, afterslip beneath the rupture patch following the 2002 M_w 7.9 Denali earthquake decayed to rates similar to that seen at Tabas within $\sim$4.5 yr of the event (Johnson et al. [2009](#)). Afterslip is thought to have decayed to near zero within 5 yr of the 1989 M_w 7.1 Loma Prieta earthquake (Segall et al. [2000](#)), although the slip-rate resolution of the available data is $\pm\sim$10 mm yr^{-1}. Although this discussion has only included a number of earthquakes chosen because of their contrasting postseismic signals, their comparison shows that there are examples of both earthquakes where the timescale of transient postseismic afterslip appears to be similar to that seen at Tabas (such as Alaska and Sefidabeh), and also others in which it is resolvably shorter. Our available range of observations prevent any firm conclusions being drawn regarding how common the timescales observed at Tabas may be, if any dependence exists on the magnitude of the causative earthquake, whether afterslip above and below the coseismic rupture patch have notably different characteristics, or if any other fault parameters play a role in determining the characteristic relaxation time. However, the comparison between Tabas and some other magnitude 7 earthquakes discussed above suggests that significant lateral variations in afterslip timescales probably do exist.

The long timescale of the postseismic motions emphasizes the importance of this transient slip in the geological evolution of the areas affected. The available data at Tabas lack the required observations early in the postseismic period to constrain the total amount of postseismic motion. However, a minimum estimate can be acquired by assuming slip at a constant 5 mm yr^{-1} rate between the earthquake in 1978 and the final data acquisition used in this study (in 2010). This estimate is $\sim$16 cm, and because postseismic afterslip is observed to markedly decay with time as the coseismic stresses are relaxed (e.g. Yu et al. [2003](#); Savage et al. [2005](#); Bruhat et al. [2011](#); Copley et al. [2012](#)), 16 cm is certainly a significant underestimate (possibly by an order of magnitude or more). Calculations based on fault-scaling laws predict $\sim$3.3 m of slip on the main coseismic fault plane at depth in the 1978 Tabas event (Walker et al. [2003](#)), and the postseismic motions may form a considerable proportion of the accommodation of this displacement at the surface (consistent with the coseismic ruptures being only up to $\sim$35 cm in magnitude (Berberian [1979](#))). These slip estimates underline the importance of postseismic afterslip in the geological evolution of fold and thrust belts similar to those at Tabas.

6 CONCLUSIONS

Postseismic afterslip imaged with InSAR following the 1978 M_w 7.3 Tabas thrust-faulting earthquake in eastern Iran provides insights into the long timescale over which postseismic afterslip can occur, and the role this deformation can play in the geological evolution of thrust belts. Slip occurred on relatively steeply dipping thrust ramps connecting growing anticlines visible at the surface with the low-angle coseismic fault plane at depth. In one location, a backthrust is also postseismically active. These results emphasise that deformation throughout the seismic cycle can contribute to the geological evolution of zones of active faulting.

REFERENCES

Allmendinger, R.W. & Shaw, J.H., 2000. Estimation of fault propagation distance from fold shape: implications for earthquake hazard assessment, *Geology,* **28,** 1099–1102.

Avouac, J.-P., Tapponnier, P., Bai, M., You, H. & Wang, G., 1993. Active thrusting along the northern Tien Shan and late Cenozoic rotation of the Tarim relative to Dzungaria and Kazakhstan, *J. geophys. Res.,* **98,** 6755–6804.

Bayasgalan, A., Jackson, J., Ritz, J.-F. & Carretier, S., 1999a. Field examples of strike-slip fault terminations in Mongolia, and their tectonic significance, *Tectonics,* **18,** 394–411.

Bayasgalan, A., Jackson, J., Ritz, J.-F. & Carretier, S., 1999b. Forebergs, flower structures, and the development of large intra-continental strike-slip faults: the Gurvan Bogd fault system in Mongolia, *J. Struct. Geol.,* **21,** 1285–1302.

Berberian, M., 1979. Earthquake faulting and bedding thrust associated with the Tabas-e-Golshan (Iran) earthquake of September 16, 1978, *Bull. seism. Soc. Am.,* **69,** 1861–1887.

Berberian, M., 1982. Aftershock tectonics of the 1978 Tabas-e-Golshan (Iran) earthquake sequence: a documented active 'thin- and thick-skinned tectonic' case, *Geophys. J. R. astr. Soc.,* **68,** 499–530.

Berberian, M., Jackson, J.A., Qorashi, M., Talebian, M., Khatib, M. & Priestley, K., 2000. The 1994 Sefidabeh earthquakes in eastern Iran: blind thrust faulting and bedding-plane slip on a growing anticline, and active tectonics of the Sistan suture zone, *Geophys. J. Int.,* **142,** 283–299.

Bruhat, L., Barbot, S. & Avouac, J.-P., 2011. Evidence for postseismic deformation of the lower crust following the 2004 Mw6.0 Parkfield earthquake, *J. geophys. Res.,* **116,** doi:10.1029/2010JB008073.

Burbank, D., Meigs, A. & Brozovic, N., 1996. Interactions of growing folds and coeval depositional systems, *Basin Res.,* **8,** 199–223.

Charreau, J., Avouac, J.-P., Chen, Y., Dominguez, S. & Gilder, S., 2008. Miocene to present kinematics of fault-bend folding across the Huerguosi anticline, northern Tianshan (China), derived from structural, seismic, and magnetostratigraphic data, *Geology,* **36,** 871–874.

Copley, A., Hollingsworth, J. & Bergman, E., 2012. Constraints on fault and lithosphere rheology from the coseismic slip and postseismic afterslip of the 2006 Mw7.0 Mozambique earthquake, *J. geophys. Res.,* **117,** doi:10.1029/2011JB008580.

Copley, A. & Reynolds, K., *Imaging topographic growth by long-lived postseismic afterslip at Sefidabeh,* east Iran, in review.

Engdahl, E.R., van der Hilst, R. & Buland, R., 1998. Global teleseismic earthquake relocation with improved travel times and procedures for depth determination, *Bull. seism. Soc. Am.,* **88,** 722–743.

Fialko, Y., 2004. Probing the mechanical properties of seismically active crust with space geodesy: study of the coseismic deformation due to the 1992 Mw7.3 Landers (southern California) earthquake, *J. geophys. Res.,* **109,** doi:10.1029/2003JB002756.

Fialko, Y., 2006. Interseismic strain accumulation and the earthquake potential on the southern San Andreas fault system, *Nature,* **441,** 968–971.

Johanson, I.A. & Burgmann, R., 2010. Coseismic and postseismic slip from the 2003 San Simeon earthquake and their effects on back-thrust slip and the 2004 Parkfield earthquake, *J. geophys. Res.,* **115,** doi:10.1029/2009JB006599.

Johanson, I.A., Fielding, E.J., Rolandone, F. & Burgman, R., 2006. Coseismic and postseismic slip of the 2004 Parkfield earthquake from space-geodetic data, *Bull. seism. Soc. Am.,* **96,** doi:10.1785/0120050818.

Johnson, K.M., Burgmann, R. & Freymueller, J.T., 2009. Coupled afterslip and viscoelastic flow following the 2002 Denali Fault, Alaska earthquake, *Geophys. J. Int.,* **176,** 670–682.

Jonsson, S., Zebker, H., Segall, P. & Amelung, F., 2002. Fault slip distribution of the 1999 Mw7.1 Hector Mine, California, earthquake, estimated from satellite radar and GPS measurements, *Bull. seism. Soc. Am.,* **92,** 1377–1389.

Keller, E.A. & Pinter, N., 2002. *Active Tectonics: Earthquakes, Uplift, and Landscape,* 2nd edn, Prentice Hall.

Keller, E.A., Gurrola, L. & Tierney, T.E., 1999. Geomorphic criteria to determine the direction of lateral propagation of reverse faulting and folding, *Geology,* **27,** 515–518.

King, G.C.P., Stein, R.S. & Rundle, J.B., 1988. The growth of geological structures by repeated earthquakes 1: conceptual framework, *J. geophys. Res.,* **93,** 13 307–13 318.

Lavé, J. & Avouac, J.P., 2000. Active folding of fluvial terraces across the Siwaliks Hills, Himalayas of central Nepal, *J. geophys. Res.,* **105,** 5735–5770.

Meyer, B., Tapponnier, P., Bourjot, L., Metivier, F., Gaudemer, Y., Peltzer, G., Shunmin, G. & Zhitai, C., 1998. Crustal thickening in Gansu-Qinghai, lithospheric mantle subduction, and oblique, strike-slip controlled growth of the Tibetan plateau, *Geophys. J. Int.,* **135,** 1–47.

Okada, Y., 1985. Surface deformation due to shear and tensile faults in a half-space, *Bull. seism. Soc. Am.,* **75**(4), 1135–1154.

Perfettini, H. & Avouac, J.-P., 2004. Postseismic relaxation driven by brittle creep: a possible mechanism to reconcile geodetic measurements and the decay rate of aftershocks, application to the Chi-Chi earthquake, Taiwan, *J. geophys. Res.,* **109,** doi:10.1029/2003JB002488.

Philip, H., Rogozhin, E., Cisternas, A., Bousquet, J.C., Borisov, B. & Karakhanian, A., 1992. The Armenian earthquake of 1988 December 7: faulting and folding, neotectonics and palaeoseismicity, *Geophys. J. Int.,* **110,** 141–158.

Rosen, P.A., Hensley, S. & Peltzer, G., 2004. Updates repeat orbit interferometry package released, *EOS, Trans. Am. geophys. Un.,* **85,** 47.

Savage, J.C., Svarc, J.L. & Yu, S.-B., 2005. Postseismic relaxation and transient creep, *J. geophys. Res.,* **110,** doi:10.1029/2005JB003687.

Scharer, K.M., Burbank, D.W., Chen, J. & Weldon, R.J., 2006. Kinematic models of fluvial terraces over active detachment folds: constraints on the growth mechanism of the Kashi-Atushi fold system, Chinese Tian Shan, *Bull. Geol. soc. Am.,* **118,** 1006–1021.

Segall, P., Burgmann, R. & Matthews, M., 2000. Time-dependent triggered afterslip following the 1989 Loma Prieta earthquake, *J. geophys. Res.,* **105,** 5615–5634.

Stein, R.S. & King, G.C., 1984. Seismic potential revealed by surface folding: 1983 Coalinga, California, earthquake, **224,** 869–872.

Suito, H. & Freymueller, J.T., 2009. A viscoelastic and afterslip postseismic deformation model for the 1964 Alaska earthquake, *J. geophys. Res.,* **114,** doi:10.1029/2008JB005954.

Talebian, M. *et al.*, 2004. The 2003 Bam (Iran) earthquake: rupture of a blind strike-slip fault, *Geophys. Res. Lett.,* **31,** doi:10.1029/2004GL020058.

Wald, D.J., Heaton, T.H. & Hudnut, K.W., 1996. The slip history of the 1994 Northridge, California, earthquake determined from strong-motion, teleseismic, GPS, and leveling data, *Bull. seism. Soc. Am.,* **86,** 49–70.

Walker, R., Jackson, J. & Baker, C., 2003. Surface expression of thrust faulting in eastern Iran: source parameters and surface deformation of the 1978 Tabas and 1968 Ferdows earthquake sequences, *Geophys. J. Int.,* **152,** 749–765.

Walker, R., Gans, P., Allen, M.B., Jackson, J., Khatib, M., Marsh, N. & Zarrinkoub, M., 2009. Late Cenozoic volcanism and rates of active faulting in eastern Iran, *Geophys. J. Int.,* **177,** 783–805.

Walker, R.T., Khatib, M.M., Bahroudi, A., Rodes, A., Schnabel, C., Fattahi, M., Talebian, M. & Bergman, E., 2013. Co-seismic, geomorphic, and geological fold growth associated with the 1978 Tabas-e-Golshan earthquake fault in eastern Iran, *Geomorphology,* doi:10.1016/j.geomorph.2013.02.016.

Wright, T., Parsons, B. & Fielding, E., 2001. Measurement of interseismic strin accumulation across the North Anatolian Fault by satellite radar interferometry, *Geophys. Res. Lett.,* **28,** 2117–2120.

Yielding, G.H., Jackson, J.A., King, G.C.P., Sinvhal, H., Vita-Finzi, C. & Wood, R.-M., 1981. Relations between surface deformation, fault geometry, seismicity, and rupture characteristics during the El Asnam (Algeria) earthquake of 10 October 1980, *Earth planet. Sci. Lett.,* **56,** 287–304.

Yu, S.-B., Hsu, Y.-J., Kuo, L.-C., Chen, H.-Y. & Liu, C.-C., 2003. GPS measurement of postseismic deformation following the 1999 Chi-Chi, Taiwan, earthquake, *J. geophys. Res.,* **108,** doi:10.1029/2003JB002396.

APPENDIX A: ADDITIONAL FAULT SLIP INVERSIONS

This appendix contains inversions supplemental to those in the main paper, as described in Section 4.

Fig. A1 shows inversion results for the profile e–e′, as with Fig. 5, but using the stack of Envisat interferograms, rather than ERS interferograms. There is a larger non-tectonic signal that must be accounted for in the inversion, and the results are less well-constrained, but the range of possible fault parameters overlaps those shown in Fig. 5.

Figs A2 and A3 show inversions of the stacks of ERS and Envisat interferograms for profile d–d′ in Fig. 2. The level of non-tectonic motion in this location in the ERS results leads to very poorly constrained fault parameters (Fig. A2). The lower limit on the depth to the base of the fault in this case is not likely to be real, but an artefact of the assumption that non-tectonic features of the data can be described by an offset plus a planar ramp, rather than a more complex shape. The results using the Envisat data are more well-constrained, due to less non-tectonic noise, and are consistent with the results from the nearby profile e–e′ discussed in the main paper.
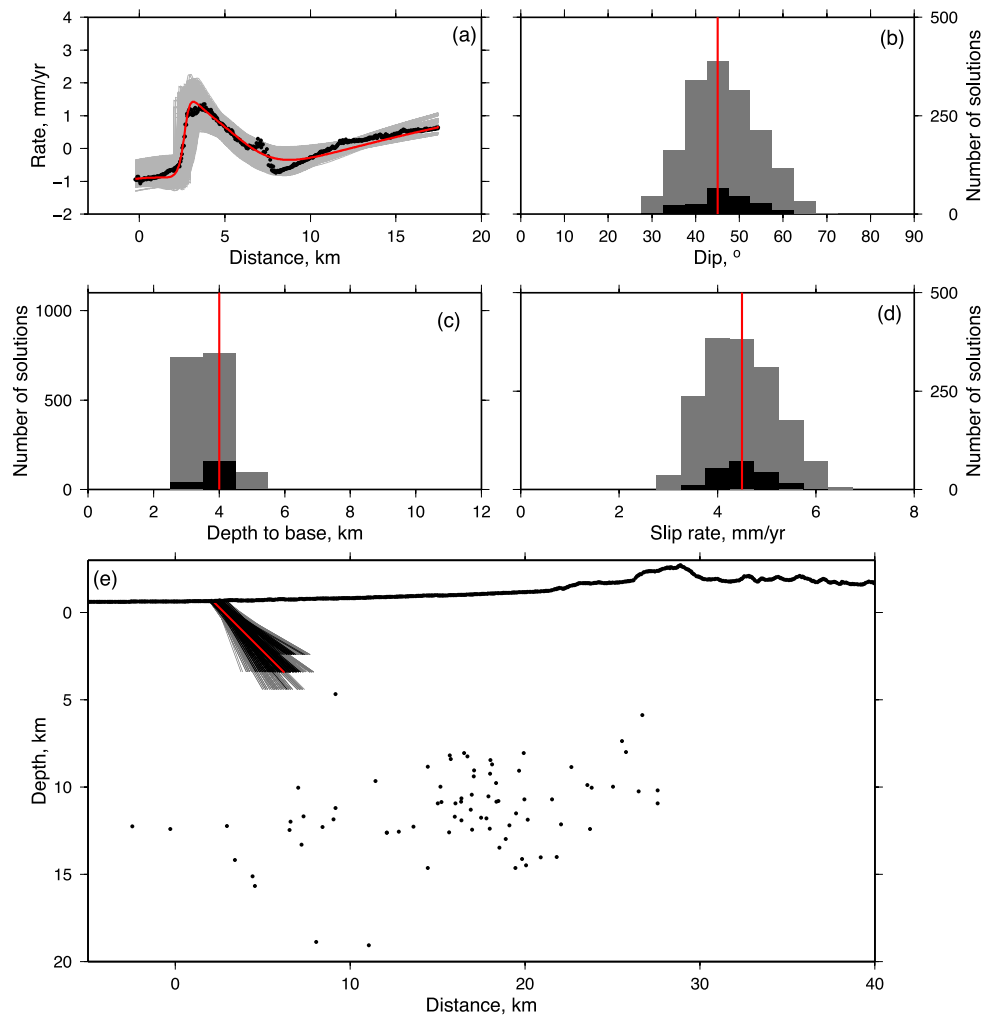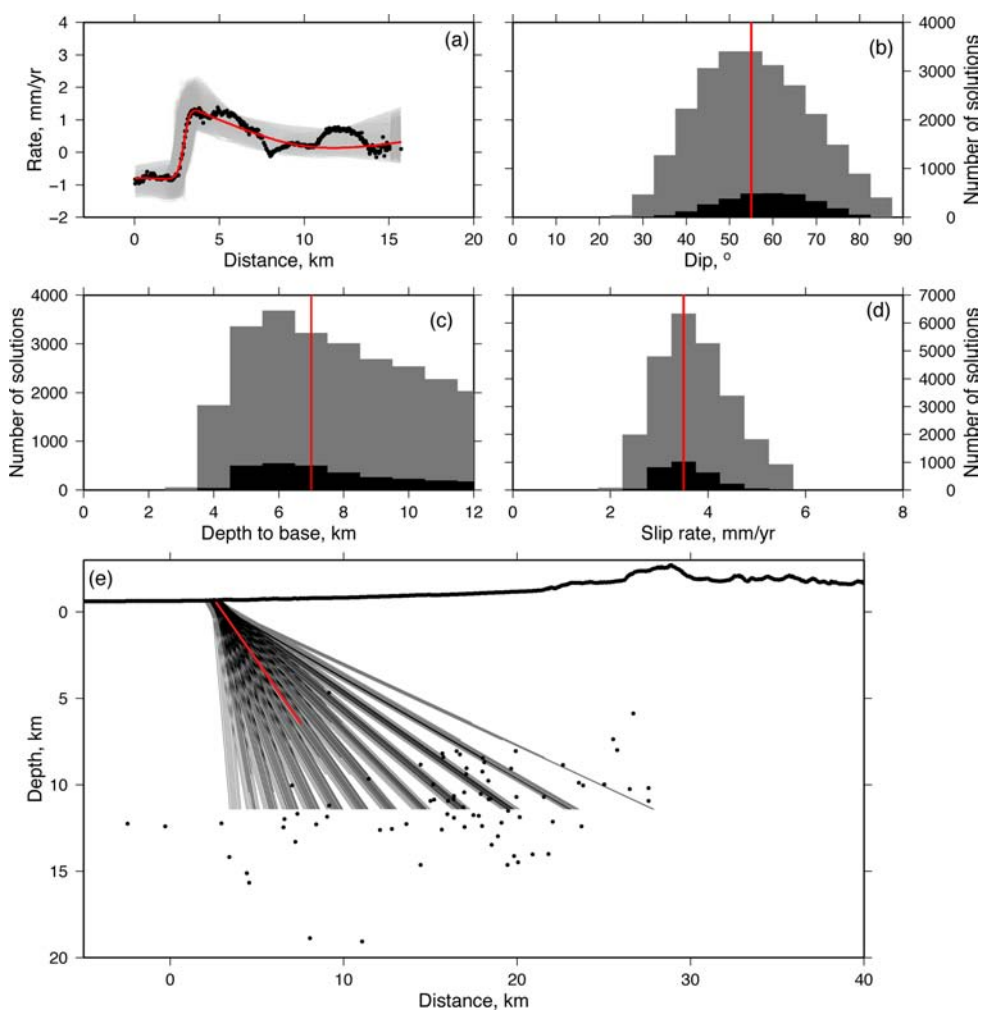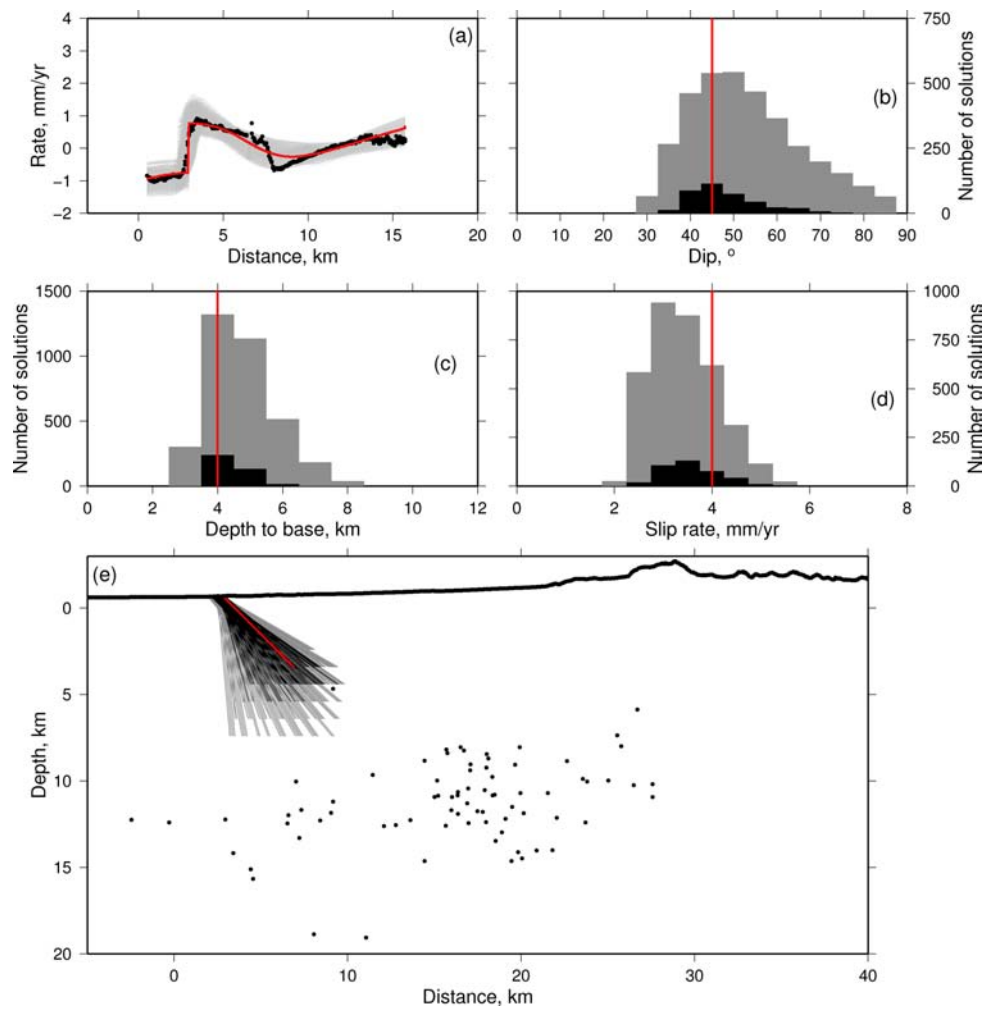
Figure A1. As for Fig. 5, but using Envisat data.

Figure A2. As for Fig. 5, but for profile d–d′ on Fig. 2 using ERS data.

Figure A3. As for Fig. 5, but for profile d–d′ on Fig. 2 using Envisat data.